Energy Migration in Dye-Loaded Hexagonal Microporous Crystals

Niklaus Gfeller and Gion Calzaferri*

Department of Chemistry and Biochemistry, University of Bern, Freiestrasse 3, CH-3000 Bern 9, Switzerland

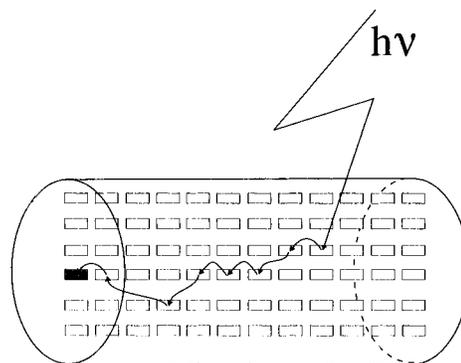*Received: September 10, 1996; In Final Form: December 3, 1996*[⊗]

Microporous materials containing linear channels running through hexagonal microcrystals allow the formation of very concentrated monomeric and highly anisotropic oriented dye systems that support extremely fast energy migration. Energy migration can be described as a homogeneous Markoffian random walk, in which each energy transfer step is incoherent and occurs from a thermalized initial state. The dyes investigated have an electronic transition dipole moment $\mu_{S_1 \leftarrow S_0}$ which coincides with their long axes. The individual energy transfer steps calculated based on dipole−dipole interactions occur with rate constants of up to 30 ps^{-1}. This fast energy migration cannot be described by a diffusive process immediately after irradiation but becomes diffusive after several tenths of a picosecond. After this time a constant diffusion coefficient D can be defined with values of up to about 0.3 cm^2 s^{-1} for an optimized system based on, for example, cylindrical zeolite L microcrystals and oxonine. A main part of this study refers to excitation trapping on the surface of cylindrical microcrystals. We distinguish between *front trapping* (traps positioned on the front of the cylinders), *front−back trapping* (traps on the front and on the back), *coat trapping* (traps on the coat), *axial trapping* (traps located in the central channel), and *point trapping* (a single trap at the center of the front). In cylindrical microcrystals with a size of 50 nm containing about 33 000 chromophores and complete coverage of the outer surface by traps, a total trapping efficiency of 99.8% can be obtained. The front−back trapping efficiency is 60.4% and the coat trapping efficiency is 39.4%. The front trapping efficiencies reach 99.0% if only the front is covered by traps. In a microcrystal of 37 nm length, still containing 12 600 chromophores, point trapping efficiencies of up to 93.0% have been calculated.

1. Introduction

The complexity and beauty of natural systems have encouraged chemists to study the structure and properties of organized media such as molecular crystals, liquid crystals, and related regular arrangements and to mimic some of their functionalities. Microporous structures containing atoms, clusters, molecules, or complexes provide a source of new materials with challenging properties.[1] Especially appealing inorganic microporous frameworks are zeolites because they possess a large variety of well-defined internal structure such as uniform cages, cavities, or channels.[2,3] Chromophore-loaded zeolites have been investigated for different purposes such as the generation of the second harmonics, of frequency doubling, and of optical bistabilities giving rise to persistent spectral hole burning.[4−8] The role of the zeolite framework is to act as a host for realizing the desired geometrical properties and for stabilizing the incorporated molecules.[9,10] Incorporation of chromophores into the zeolites can be achieved in different ways, depending on the substances used and on the desired properties: from the gas phase,[11,12] by ion exchange if cations are involved,[13] by crystallization inclusion,[9] or by performing an *in situ* synthesis inside of the zeolite cages.[14]

One can speculate on using strongly luminescent dye molecules organized by a well-chosen zeolite host to mimic important properties of the natural antenna system of green plants, which consists of several hundred chlorophyll molecules closely packed in a hydrophobic environment. The spectral properties of the chlorophyll molecules and the small distances between them favor fast relocation of electronic excitation from an excited species to an unexcited neighbor. Electronic excitation is transported very fast through the antenna until it reaches

SCHEME 1: Schematic View of an Artificial Antenna (Dye Molecules Are Located at Sites Indicated by Rectangles; The Rectangle Containing the Trap Is Shaded)

the reaction center, where further steps of photosynthesis take place. It has been reported that the anisotropic arrangement of chlorophyll molecules is important for efficient energy migration.[15]

A schematic view of the antenna envisaged in this study is illustrated in Scheme 1. The monomeric dye molecules are represented by rectangles. The dye molecule that has been excited by absorbing an incident photon transfers electronic excitation to another one. After a series of such steps the electronic excitation reaches the trap, which we have pictured as a shaded rectangle. The energy migration is in competition with spontaneous emission, radiationless decay, and photochemically induced degradation. Very fast energy migration is therefore crucial if a trap should be reached before other processes can take place. The energy quantum can be guided to the next reaction step once it has been captured by the trap.

Dye-Loaded Hexagonal Microporous Crystals

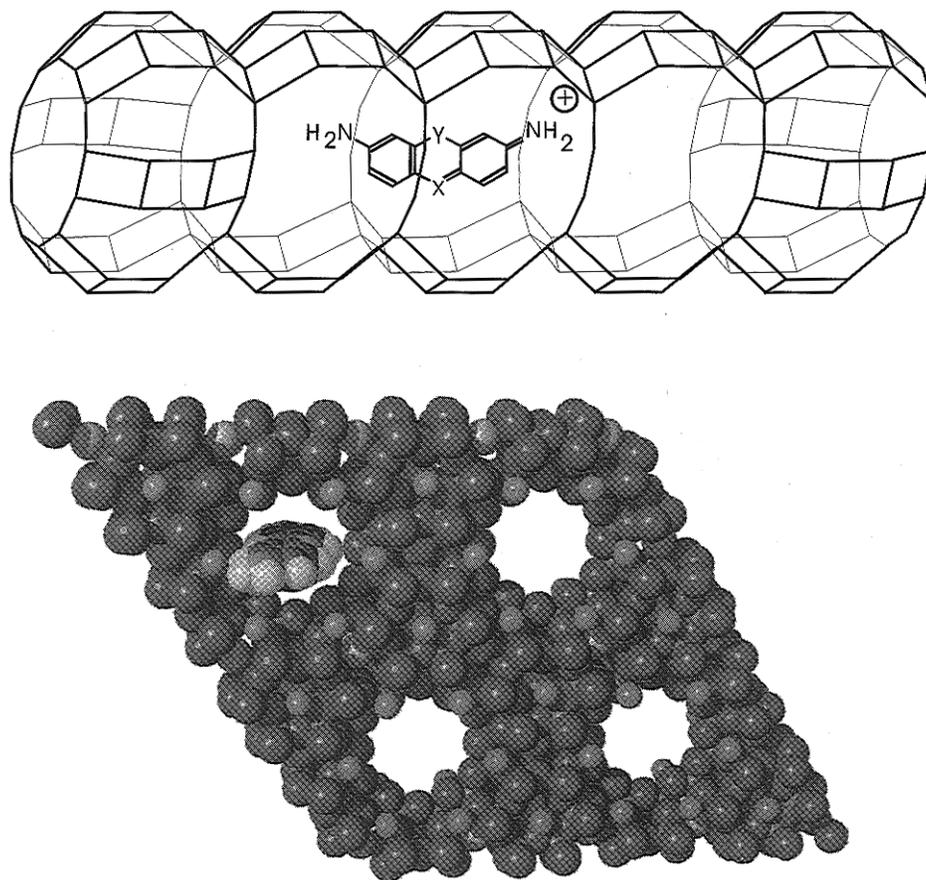*J. Phys. Chem. B, Vol. 101, No. 8, 1997* **1397**

Figure 1. Structure of zeolite L and of dye molecules inside a channel and a space-filling model.

These conditions impose not only spectroscopic but also decisive geometrical constraints on the system.

Imaginative attempts different from ours have been presented in the literature to build an artificial antenna. Multinuclear luminescent metal complexes,[16,17] multichromophore cyclodextrins,[18] Langmuir−Blodgett films,[19−22] and dyes in polymer matrices[23−25] have been investigated. Some sensitization processes in silver halide photographic materials[26] and also the spectral sensitization of polycrystalline titanium dioxide films bear in some cases aspects of artificial antenna systems.[27,28]

By analogy with the natural antenna systems we deduce that favorable conditions for realizing an efficient device as illustrated in Scheme 1 are a high concentration of monomeric dye molecules with a large Förster energy transfer radius, high luminescence quantum yield, ideal geometrical arrangement of the chromphores, and an optimal size of the device. Dyes at high concentration usually have the tendency to form aggregates which in general show very fast radiationless decay.[29] In natural antenna systems the formation of aggregates is prevented by fencing the chlorophylls in polypeptide cages.[30] A similar approach is possible by enclosing dyes inside a microporous material and by choosing conditions such that the volume of the cages and channels is only able to uptake monomers but not aggregates. Materials bearing linear channels running through microcrystals allow the formation of highly anisotropic dye assemblies. Examples of zeolites bearing such channels, large enough to uptake organic dye molecules, which are especially attractive for this aim, are reported in Table 1.[3] A few cases based on zeolite L as a host and the cationic dye molecules pyronine and oxonine as chromophores have been investigated experimentally to some extent for this purpose.[31] Thionine was found to be a good candidate for studying space-filling properties and isothermal ion exchange relevant in these

TABLE 1: Lattice Constants *a*, *b*, and *c* and Free Opening Diameters ⊘ of Hexagonal and Orthorhombic Structures with Linear Channels (in Å)[3]

	a	*b*	*c*	⊘
Hexagonal				
mazzite	18.4		7.6	7.4
AlPO$_4$-5	13.4		8.4	7.3
zeolite L	18.4		7.5	7.1
gmelinite	13.8		10	7
offretite	13.3		7.6	6.8
CoAPO-50	12.8		9	6.1
cancrinite	12.8		5.1	5.9
Orthorhombic				
AlPO$_4$-11	13.5	18.5	8.4	6.3/3.9[a]
mordenite	18.1	20.5	7.5	7.0/6.5[a]

[a] Major and minor axis of the elliptic cross section.

studies.[13] We show in Figure 1 a side view and a space-filling top view of the zeolite L together with these dye molecules. While the dye molecules can penetrate the channels, formation of dimers inside of them is not possible. The normalized absorption and emission spectra of pyronine and oxonine in zeolite L are given in Figure 2. The spectral overlap between the absorption and the emission spectra of both dyes, which bear very high luminescence quantum yields, is indicated by the shaded regions. We should add that zeolite L microcrystals with sizes ranging from 20 nm to about 1 μm, with cylinder morphology and varying length to diameter ratios ranging from a disk to a cigar-like shape, have been recently prepared.[32,33]

In the present work, energy migration among dye molecules arranged anisotropically inside such microporous materials is studied theoretically. Energy migration in one-dimensional,[34] two-dimensional,[35−37] and in three-dimensional systems[38−42] has been treated analytically for ordered and disordered systems. We prefer a numerical treatement of energy migration on the
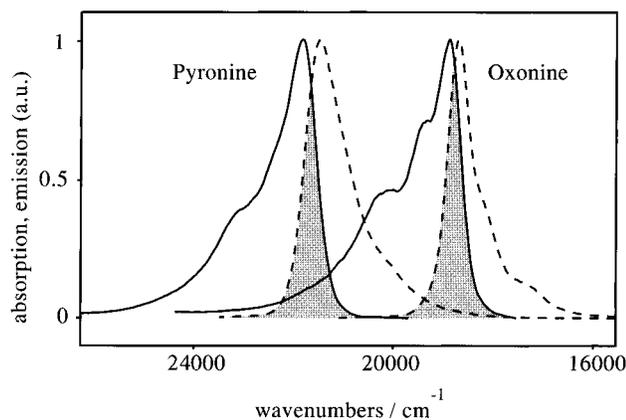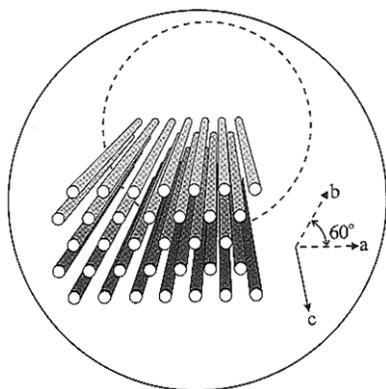
Figure 2. Absorption (solid) and corrected emission (dotted) spectra of Py−L and Ox−L zeolites suspended in water. The exchange degree θ of both samples was 0.004. The maxima of all spectra were adjusted to equal height. The spectral overlap of the two dyes is marked as gray area.

SCHEME 2: Schematic View of Some Channels in a Hexagonal Zeolite Microcrystal

basis of stochastic processes in which each energy transfer step is incoherent and occurs from a thermalized initial state.[43] This leads to remarkable insight into the processes occurring in the system. Special attention has been paid to the description of the probability that an electronic excitation initially being at a chromophore inside of the cylindrical microcrystal reaches traps positioned at a specific place on the outer surface.

2. Description of the System

2.1. Basic Assumptions. We describe the antenna properties of a system consisting of dye molecules in hexagonally arranged linear channels. Materials providing such channels are reported in Table 1. We investigate a cylindrical shape as illustrated in Scheme 2, where some channels and the coordinate system are indicated. The primitive vector **c** corresponds to the channel axis, while the primitive vectors **a** and **b** are perpendicular to it, enclosing an angle of 60°. The channels run parallel to the central axis of the cylinder.[33] The length and radius of the cylinder are l_{cyl} and r_{cyl}, respectively. The theory reported is based on a few assumptions that are supported by experiments carried out on cationic dye molecules in zeolite L.[13,31] The description of the processes is simplified by referring to a large number of microcrystals with a narrow distribution of size and shape.

(a) The dye molecules are positioned at sites fixed along the linear channels. The sites do not overlap. The length of a site is equal to an integral number u times the length of **c**, so that one dye molecule fits into one site. The number u depends on the size of the dye molecules and on the length of the primitive

unit cell. As an example, pyronine and oxonine (length ≈ 15 Å) in zeolite L ($|\mathbf{c}| = 7.5$ Å) require two primitive unit cells per molecule; therefore u is equal to 2. The sites form a new Bravais lattice with the primitive vectors **a**, **b**, and $u\mathbf{c}$.

(b) Two types of sites exist. The first one can be occupied with dye molecules and is marked with small letters. The second type, marked with capital letters, is reserved for traps. Per microcrystal, the number of sites available for dye molecules is i_{max} and the number of sites available for traps is I_{max}. Both types of sites have the same geometrical properties. All dye molecules in sites i are assumed to be identical. This is achieved by averaging over the thermal distribution. The same is valid for traps.

(c) Only dye molecules with a large electronic transition dipole moment $\mu_{S_1 \leftarrow S_0}$ are taken into account. This means that the $S_1 \leftarrow S_0$ transition is of $\pi^* \leftarrow \pi$ type. It is assumed that the radiationless energy transfer between excited and unexcited molecules can be described by the dipole−dipole mechanism, the so-called Förster mechanism.[44]

(d) The dye molecules are chosen such that their long axis coincides with the channel axis **c**. Hence, their short axes can occupy all directions perpendicular to **c**. We discuss cases where the relevant electronic transition dipole moment of the dye molecules coincides with their long axes. Therefore, both absorbed and emitted photons flow perpendicular to the **c** axis of the microcrystals.

(e) Each site i is occupied with the same probability p_i by a dye molecule. The occupation probability p_i is equal to the ratio between the occupied and the total number of sites. In cases where cationic dye molecules are intercalated by ion exchange, p_i is proportional to the exchange degree θ, which is defined as the ratio of dye molecules and exchangeable cations. $[K^+]_Z$ is the number of exchangeable cations per unit cell, and the relation between the exchange degree θ and the occupation probability p_i is given by[13]

$$p_i = u[K^+]_Z \theta \tag{1}$$

The occupation probability p_I of sites I is treated in an analogous way.

(f) Each site i of a given microcrystal has the same probability P_i of being occupied by an electronically excited molecule, immediately after irradiation with a Dirac pulse. The excitation probability P_i of site i is the ith element of a vector **P**, which we call excitation distribution among the sites. We restrict the discussion to the low-intensity case in which at maximum one dye molecule per microcrystal is in an electronically excited state. This means that intensity dependent processes such as, for example, stimulated emission do not occur.

(g) We do not consider radiationless decay pathways of the excited dye molecules. This would be easy to include, but we are interested in dye molecules with a luminescence quantum yield of 1 or close to 1. Pyronine and oxonine are examples which fulfill this condition well.[31] Self-absorption and reemission processes are of minor importance for the experimental conditions envisaged. They are therefore not discussed.

2.2. Coordinates of the Sites. As mentioned before, the sites form a Bravais lattice, where the position $\mathbf{R}_i$ of a site i is expressed by the primitive vectors **a**, **b**, and $u\mathbf{c}$ of the hexagonal lattice and the integers $n_a^{(i)}$, $n_b^{(i)}$, and $n_c^{(i)}$.

$$\mathbf{R}_i = n_a^{(i)}\mathbf{a} + n_b^{(i)}\mathbf{b} + n_c^{(i)}u\mathbf{c} \tag{2}$$

Sites with equal n_c belong to slabs cut perpendicular to the **c** axis. This is illustrated in Figure 3. The first slab $n_c = 0$ is situated on the front and the last slab $n_c = n_c^{max}$ on the back of
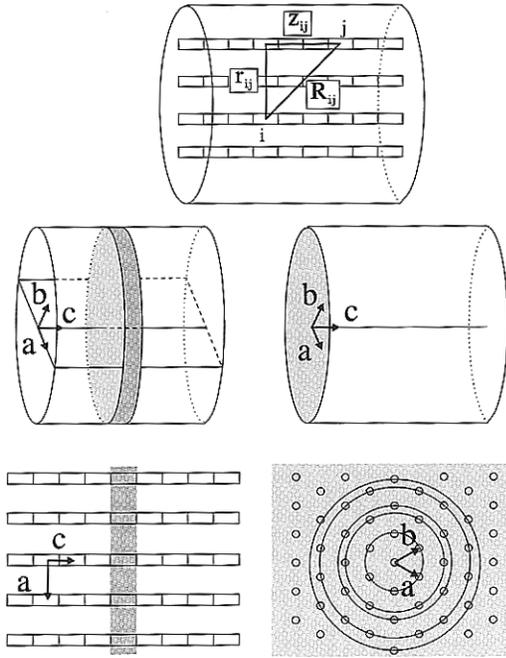
Dye-Loaded Hexagonal Microporous Crystals

J. Phys. Chem. B, Vol. 101, No. 8, 1997 **1399**

Figure 3. Geometrical arrangement of the antenna. The sites are marked by rectangles. (Top) Definition of the distances R_{ij}, r_{ij} and z_{ij} between sites i and j. (Left) Cut through the center of the cylindrical microcrystal along **a** and **c**. The sites of the shaded area belong to one slab. (Right) Cut vertical to **c**. The channels indicated by circles are arranged in rings around the central channel because of the hexagonal symmetry.

the cylinder. The total number of slabs n_c^{max} depends on the length l_{cyl} of the cylindrical microcrystal.

$$n_c^{max} = l_{cyl}/u|\mathbf{c}| \tag{3}$$

The distance z of a slab n_c from the front side is equal to $n_c u |\mathbf{c}|$. The channels are characterized by the numbers (n_a, n_b); hence, sites with the same (n_a, n_b) values belong to the same channel. n_a and n_b are both equal to zero for the central channel, which coincides with the cylinder axis. The values of n_a and n_b are limited by the radius of the cylinder r_{cyl} and range from $-n_r^{max}$ to n_r^{max}:

$$n_r^{max} = \frac{r_{cyl}}{|\mathbf{a}|} \tag{4}$$

The distance r between a channel (n_a, n_b) and the central channel is given by $r = |n_a \mathbf{a} + n_b \mathbf{b}|$. Thus, the possible range of the (n_a, n_b) is further limited by the condition $|n_a \mathbf{a} + n_b \mathbf{b}| \leq r_{cyl}$. Because of the hexagonal symmetry, **a** and **b** have equal lengths and the angle between **a** and **b** is 60°. The length r of the vector $n_a \mathbf{a} + n_b \mathbf{b}$ is therefore calculated as follows:

$$r = |\mathbf{a}|\sqrt{(n_a + n_b \cos 60)^2 + (n_b \sin 60)^2} =$$
$$|\mathbf{a}|\sqrt{n_a^2 + n_a n_b + n_b^2} \tag{5}$$

Rings consisting of six channels can be formed, due to the hexagonal symmetry, as illustrated in Figure 3. The six channels all have the same distance from the center (0,0). Each ring is represented by the channel $(n_a^{(0)}, n_b^{(0)})$ with $n_a^{(0)} > 0$, $n_b^{(0)} \geq 0$. The remaining five channels $(n_a^{(m)}, n_b^{(m)})$ are found by applying the transformation T to $(n_a^{(0)}, n_b^{(0)})$ m times ($m = 1, 2, ..., 5$). T corresponds to a rotation of 60°. In some cases two, three or four 6-rings are located on the same circle but displaced by a certain angle, due to the hexagonal symmetry. The tubes of

each of these 6-rings, however, behave in the same way.

$$(n_a^{(m)}, n_b^{(m)}) = (n_a^{(0)}, n_b^{(0)})T^m \quad \text{with} \quad T = \begin{pmatrix} 1 & -1 \\ 1 & 0 \end{pmatrix} \tag{6}$$

The probability for an energy transfer between two sites i and j strongly depends on the vector $\mathbf{R}_{ij}$ which is characterized by

$$\mathbf{R}_{ij} = (n_a^{(i)} - n_a^{(j)})\mathbf{a} + (n_b^{(i)} - n_b^{(j)})\mathbf{b} + (n_c^{(i)} - n_c^{(j)})u\mathbf{c} \tag{7}$$

$$R_{ij} = \sqrt{r_{ij}^2 + z_{ij}^2} \tag{8}$$

where z_{ij} and r_{ij} are the distances between the slabs and the channels to which the two sites belong. They correspond to the distances between the sites along and perpendicular to **c**, respectively. The vectors $\mathbf{R}_{ij}$, $\mathbf{z}_{ij}$, and $\mathbf{r}_{ij}$ are indicated in Figure 3.

$$r_{ij} =$$
$$|\mathbf{a}|\sqrt{(n_a^{(i)} - n_a^{(j)})^2 + (n_a^{(i)} - n_a^{(j)})(n_b^{(i)} - n_b^{(j)}) + (n_b^{(i)} - n_b^{(j)})^2} \tag{9}$$

$$z_{ij} = u|\mathbf{c}|(n_c^{(i)} - n_c^{(j)}) \tag{10}$$

2.3. Förster's Theory of Energy Transfer. According to Förster,[44] the rate constant k_{ij} for energy transfer from an excited dye molecule on site i to an unexcited one on site j depends on the fluorescence quantum yield Φ_i of the donor in the absence of acceptors and on its natural lifetime τ_i, on the refractive index n of the medium, on the geometrical factor G_{ij}, which will be derived below, on the spectral overlap J_{ij} of the donor emission and the acceptor absorption spectra, and on the occupation probabilities p_i and p_j of the respective sites. N_A is the Avogadro number.

$$k_{ij} = \frac{9000(\ln 10)}{128\pi^5 N_A n^4} \frac{\Phi_i}{\tau_i} G_{ij} J_{ij} p_i p_j \tag{11}$$

The rate constant k_{iI} for energy transfer from site i to site I is analogously calculated by replacing p_j by P_I and J_{ij} by J_{iI}. The spectral overlap J_{ij} is equal to the integral of the corrected and normalized fluorescence intensity $f_i(\nu)$ of the donor multiplied by the extinction coefficient $\epsilon_j(\nu)$ of the acceptor:

$$J_{ij} = \int_0^\infty \epsilon_j(\nu) f_i(\nu) \frac{d\nu}{\nu^4} \tag{12}$$

All J_{ij} are equal, because all dye molecules are identical. The spectral overlap J_{iI} between donors and traps is calculated in the same way. The traps are assumed to have the same spectral properties, and hence all J_{iI} have the same numerical values. Furthermore the p_i and p_I are constant for all sites i and I, respectively. The energy transfer rate constants k_{ij} between all site pairs ij are proportional to the product of p_i^2 and J_{ij}. The rate constants k_{iI} for transitions from any site i to any site I are proportional to the product of $p_i p_I$ and J_{iI}.

$$k_{ij} \propto p_i^2 J_{ij}$$
$$k_{iI} \propto p_i p_I J_{iI} \tag{13}$$

Supposing there are two systems, the first one determined by $p_i^{(1)}$ and $J_{ij}^{(1)}$, the second one by $p_i^{(2)}$ and $J_{ij}^{(2)}$. Thus, the following relations hold between $k_{ij}^{(1)}$ and $k_{ij}^{(2)}$ and between $k_{iI}^{(1)}$ and $k_{iI}^{(2)}$:

$$k_{ij}^{(2)} = k_{ij}^{(1)} \frac{(p_i^{(2)})^2 J_{ij}^{(2)}}{(p_i^{(1)})^2 J_{ij}^{(1)}}$$

$$k_{iI}^{(2)} = k_{iI}^{(1)} \frac{p_i^{(2)} p_I^{(2)} J_{iI}^{(2)}}{p_i^{(1)} p_I^{(1)} J_{iI}^{(1)}} \qquad (14)$$

The geometrical factor G_{ij} takes care of the influence of the geometrical arrangement of a donor i and an acceptor j. It depends on the distance $\mathbf{R}_{ij}$ and on κ_{ij}, which describes the relative orientation in space of the transition dipole moments $(\mu_{S_1 \leftarrow S_0})_i$ and $(\mu_{S_1 \leftarrow S_0})_j$ of the donor i and of the acceptor j, respectively.

$$G_{ij} = \kappa_{ij}^2 / R_{ij}^6 \qquad (15)$$

κ_{ij} depends on the angles θ_i, θ_j, and ϕ_{ij} between the electronic transitions dipole moments, which are defined in Scheme 3.

$$\kappa_{ij} = \sin\theta_i \sin\theta_j \cos\phi_{ij} - 2\cos\theta_i \cos\theta_j \qquad (16)$$

The geometrical constraints imposed on the system lead to a simplification of eq 16 since all transition dipole moments are parallel to the **c** axis, and hence, we can write $\theta_i = \theta_j = \theta_{ij}$ and $\phi_{ij} = 0$. The angles θ_{ij} depend on both distances, z_{ij} and r_{ij}. They can be expressed as

$$\sin\theta_{ij} = r_{ij}/R_{ij}$$

$$\cos\theta_{ij} = z_{ij}/R_{ij} \qquad (17)$$

The angle θ_{ij} is zero for transitions along z, and it is equal to $\pi/2$ for transitions along r. This leads to the following expression for the orientation factor κ_{ij}:

$$\kappa_{ij} = \frac{r_{ij}^2 - 2z_{ij}^2}{R_{ij}^2} \qquad (18)$$

The geometrical situation and the angular dependence of κ^2, as calculated from eq 18 and for isotropic conditions, are illustrated in Scheme 4. The value of κ^2 for energy transfer along the **c** axis is 4 times larger than for energy transfer perpendicular to it, and it is 6 times larger than under isotropic conditions, for which one finds $\kappa^2 = 0.66$.

The geometrical factor G_{ij} can be expressed as a function of the distances r_{ij} and z_{ij} by inserting eqs 8 and 18 into eq 15:
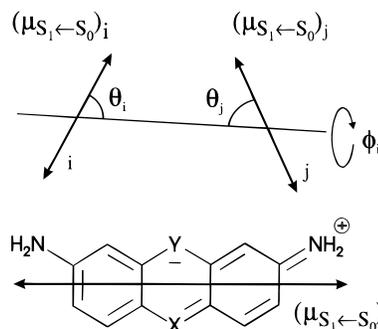
$$G_{ij} = \frac{r_{ij}^2 - 2z_{ij}^2}{(r_{ij}^2 + z_{ij}^2)^5} \qquad (19)$$

2.4. Energy Migration. Immediately after irradiation at $t = 0$ all sites i have the same excitation probability $P_i(0)$, while the traps are unoccupied, $P_I(0) = 0$. These probabilities, however, change with time because of energy migration and trapping. The excitation probability $P_i(t)$ is governed by the following master equation:
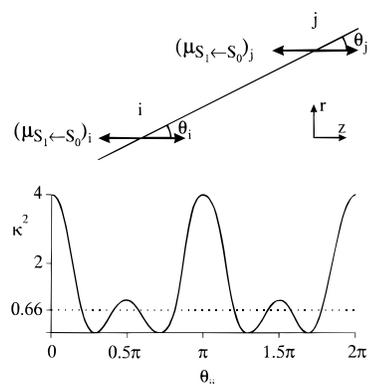
$$\frac{dP_i(t)}{dt} = \sum_j P_j(t)k_{ji} - P_i(t)k_i \qquad (20)$$

The sites i are populated by energy transfer starting from any other site j; the corresponding rate constants are k_{ji}. They are depopulated by fluorescence and by energy transfer to all sites $j \neq i$ and to trapping sites I. k_{ij} and k_{iJ} are the rate constants for energy transfer from a site i to a site j or I, respectively; see

SCHEME 3: Angles θ_i, θ_j, and ϕ_{ij}, Describing the Relative Orientation of the Transition Dipole Moment $\mu_{S_1 - S_0}$ between Two Dye Molecules Such as Pyronine (Y = O, X = CH) and Oxonine (Y = O, X = N)

SCHEME 4: (Top) Angles θ_i and θ_j between the Transition Dipole Moments of Dye Molecules at Sites in Linear Channels; (Bottom) Angular Dependence of the Orientation Factor κ^2 under Anisotropic (Solid) and under Isotropic Conditions (Dotted)

eq 11. k_F is the rate constant for fluorescence. Thus, the rate constant k_i for the depopulation is given by

$$k_i = k_F + \sum_{j \neq i} k_{ij} + \sum_J k_{iJ} \qquad (21)$$

We define the energy migration rate constant k_i^E as the sum of the individual rate constants k_{ij}. The energy migration rate constant indicates how fast site i is depopulated by energy transfer to any other site j. From this, it depends on the position of the site i, of course. To determine the energy migration rate constant, we choose a site i in the center of the microcrystal.

$$k_i^E = \sum_{j \neq i} k_{ij} \qquad (22)$$

The traps are considered a sink for the electronic excitation. This can be expressed as follows:

$$\frac{dP_I(t)}{dt} = \sum_i k_{iI} P_i(t) \qquad (23)$$

Thus, the time development of the excitation probabilities $p_i(t)$ and $P_I(t)$ is determined by eqs 20 and 23. This allows us to write the excitation probabilities valid for time $t + \Delta t$ as follows:

$$P_i(t + \Delta t) = P_i(t) + \frac{dP_i(t)}{dt}\Delta t \qquad (24)$$

Δt is considered to be small enough so that higher order terms can be neglected. Combining eqs 20 and 24 leads to the

Dye-Loaded Hexagonal Microporous Crystals

J. Phys. Chem. B, Vol. 101, No. 8, 1997 **1401**

following homogeneous Markoff chain:

$$P_i(t + \Delta t) = P_i(t) - P_i(t)k_i\Delta t + \sum_i P_j(t)k_{ji}\Delta t$$

$$P_i(t + \Delta t) = P_i(t)(1 - k_i\Delta t) + \sum_i P_j(t)k_{ji}\Delta t \quad (25)$$

The Markoff chain that describes the trapping can be expressed analogously by combining eqs 23 and 24.

$$P_I(t + \Delta t) = P_I(t) + \sum_i P_i(t)k_{iI}\Delta t \quad (26)$$

Starting from the excitation distribution $\mathbf{P}_t$ at time t after the irradiation, we calculate $\mathbf{P}_{t+\Delta t}$ at any time $t + \Delta t$ as follows.

$\mathbf{M}$ is the Markoff matrix with the following elements:

$$\mathbf{P}_{t+\Delta t} = \mathbf{P}_t \cdot \mathbf{M} \quad (27)$$

$$M_{ii} = 1 - k_i\Delta t$$

$$M_{ij} = k_{ij}\Delta t$$

$$M_{iI} = k_{iI}\Delta t$$

$$M_{Ii} = 0$$

$$M_{IJ} = 0$$

$$M_{II} = 1 \quad (28)$$

The physical meaning of the matrix elements is easy to understand. M_{ii} is the probability that the electronic excitation remains at site i. M_{ij} is the probability for a jump from site i to site j. M_{iI} is the probability for a jump from site i to site I. The probability for a jump starting at site I, M_{Ii} and M_{IJ}, is zero. The same fact is expressed by $M_{II} = 1$. The dimension of the square matrix $\mathbf{M}$ equals the number of sites per microcrystal, namely, $i_{max} + I_{max}$. The excitation distribution $\mathbf{P}_t$ valid after n time steps Δt following the irradiation at $t = 0$ is calculated as follows:

$$\mathbf{P}_t = \mathbf{P}_0 \cdot \mathbf{M}^n \quad \text{with} \quad t = n\Delta t \quad (29)$$

2.5. Trapping Efficiencies. $T(t)$ is the probability that the electronic excitation has reached a trap during the time period t after irradiation. Hence, it is equal to the sum of the excitation probabilities $P_I(t)$ of all trapping sites I at this time.

$$T(t) = \sum_I P_I(t) \quad (30)$$

The trapping rate dT/dt is given by the sum of energy transfer rates from any site i to any site I.

$$\frac{dT(t)}{dt} = \sum_i \sum_I P_i(t)k_{iI} \quad (31)$$

The trapping efficiency T_∞ is equal to the sum of the excitation probabilities of all trapping sites I at infinite time after irradiation.

$$T_\infty = \lim_{t\to\infty} T(t) = \lim_{t\to\infty} \sum_I P_I(t) \quad (32)$$

The remaining excitation $P^{tot}(t)$ corresponds to the probability that the electronic excitation is still on any site i. Hence, it is

equal to the sum of the excitation probabilities $P_i(t)$. $P^{tot}(t)$ tends towards zero when t goes to infinity.

$$P^{tot}(t) = \sum_i P_i(t)$$

$$\lim_{t\to\infty} \sum_i P^{tot}(t) = 0 \quad (33)$$

It is convenient to distinguish between different types of trapping, which we name according to the position of the traps: *Front trapping* $T_F(t)$ refers to traps positioned only on the front side of the cylindrical microcrystals. Thus, they are found in the slab $n_c = 0$. *Front−back trapping* $T_{FB}(t)$ refers to traps on the front and to traps on the back positioned in the slab $n_c = 0$ and $n_c = n_c^{max}$, respectively. *Coat trapping* $T_C(t)$ refers to traps positioned on the coat of the cylinder; this means in the outermost channels having a distance to the central channel between $r_{max} - |\mathbf{a}|$ and r_{max}. *Axial trapping* $T_A(t)$ refers to traps located in the central channel. Finally, *point trapping* $T_P(t)$ refers to a single trap positioned at the center of the front side. All these trapping types reflect symmetry aspects of the cylinder investigated. Front−back trapping and front trapping are governed by energy migration along $\mathbf{c}$, while coat trapping and axial trapping are governed by energy migration perpendicular to it. Point trapping depends on both directions of energy migration.

The fluorescence rate dF/dt as a function of time is equal to the fluorescence decay curve of the system. It is given by

$$\frac{dF(t)}{dt} = \sum_i P_i(t)k_F \quad (34)$$

The fluorescence rate constant k_F is equal for all sites i. The integrated fluorescence $F(t)$ is equal to the probability that the electronic excitation has left the system by fluorescence at time t after irradiation. It is thus equal to the probability that electronic excitation is neither on a site i nor on a site I, since radiationless decay of the dye molecules is assumed to be negligible.

$$F(t) = 1 - \sum_i P_i(t) - \sum_I P_I(t) \quad (35)$$

The fluorescence quantum yield Φ_F is simply

$$\Phi_F = 1 - T_\infty \quad (36)$$

2.6. Details of Calculation. Normally fluorescence and at least one trapping type compete with each other. This means that the competition between the different processes must be considered. We continue as follows: In a first step the different decay types are treated independently. The so obtained decay functions are $F^S(t)$, $T^S_{FB}(t)$, $T^S_C(t)$, $T^S_A(t)$, and $T^S_F(t)$. In the next step the competition between the different processes is taken into account.

The independent processes are treated as follows.

Fluorescence. In the absence of trapping processes, loss of electronic excitation is governed by the fluorescence rate constant k_f, which is equal for all sites i. Hence, the probability $P_i(t)$ decreases exponentially, and the probability $F^S(t)$ that electronic excitation has left the system by fluorescence is given by

$$F^S(t) = 1 - \sum_i P_i(0)e^{-tk_F} = 1 - e^{-tk_F} \quad (37)$$

Front−Back and Front Trapping. In these two types of trapping whole slabs are reserved for traps. We mark them with a capital letter as before. Slabs with dye molecules are marked with a small letter. Calculation of these trapping types requires only knowledge of the excitation distribution $\mathbf{Pz}_t$ along $\mathbf{c}$. The excitation distribution $\mathbf{Pz}_t$ contains the excitation probabilities $Pz_i(t)$ of the whole slabs i, which is equal to the sum of the occupation probabilities of all sites $n_c^{(i)}$ belonging to slab i. The time evolution of $\mathbf{Pz}$ is based on energy migration along $\mathbf{c}$. The energy transfer rate constant kz_{ij} from slab i to slab j is described by the sum of the rate constants for energy transfer starting from site $(0,0)$ in slab i to any site (n_a, n_b) in slab j. This simplifies the reasoning without loss of information.

$$kz_{ij} = \sum_{\text{all } (n_a,n_b) \text{ pairs}} k(z_{ij}, r(n_a, n_b)) \tag{38}$$

The rate constant kz_{iI} for energy transfer from slab i to slab I is calculated analogously, but based on the rate constants k_{iI}. The time evolution of $Pz_i(t)$ and $Pz_I(t)$ is calculated according to eqs 25 and 26, respectively.

$$Pz_i(t + \Delta t) = Pz_i(t)\Big(1 - \sum_j kz_{ij}\Delta t\Big) + \sum_j Pz_j(t)kz_{ji}\Delta t \tag{39}$$

$$Pz_I(t + \Delta t) = Pz_I(t) + \sum_i Pz_i(t)kz_{iI}\Delta t \tag{40}$$

The excitation distribution $\mathbf{Pz}_t$ among the slabs is then calculated according to (27), but here the matrix $\mathbf{Mz}$ is used instead of the matrix $\mathbf{M}$.

$$\mathbf{Pz}_t = \mathbf{Pz}_0 \cdot (\mathbf{Mz})^n \quad \text{with} \quad t = n\Delta t \tag{41}$$

The matrix $\mathbf{Mz}$ has the same form as $\mathbf{M}$, see eq 28, but the rate constants k_{ij} and k_{iI} are substituted by kz_{ij} and kz_{iI}, respectively. As before, Mz_{Ii} and Mz_{IJ} are equal to 0 and Mz_{II} equals 1. The dimension of the square matrix $\mathbf{Mz}$ is $n_c^{max} + 1$, which is the number of slabs per microcrystal. The traps are situated in slab 0 for front trapping, as mentioned before. The independent front trapping function $T^S_F(t)$ is thus equal to the excitation probability $Pz_0(t)$. For front−back trapping, traps are located in the slabs 0 and n_c^{max}. $T^S_{FB}(t)$ is therefore equal to the sum of the excitation probabilities in both slabs at time t.

$$T^S_F(t) = Pz_0(t)$$

$$T^S_{FB}(t) = Pz_0(t) + Pz_{n_c^{max}}(t) \tag{42}$$

Coat Trapping and Axial Trapping. In these types of trapping the traps are arranged in rings I. Their treatment requires knowledge of the radial excitation distribution $\mathbf{Pr}_t$. The excitation probabilities $Pr_i(t)$ of the rings i, reserved for dye molecules, and $Pr_I(t)$ of the rings I, reserved for traps, are the elements of the radial excitation distribution. One ring consists of six channels, all having the same distance r to the central channel, as illustrated in Figure 3. Thus, $Pr_i(t)$ is the sum of the occupation probabilities of all sites belonging to the channels $(n_a^{(m)i}, n_b^{(m)i})$ $(m = 0, 1, ..., 5)$ of ring i. The energy transfer rate constant kr_{ij} from ring i to ring j is equal to the sum of the rate constants of energy transfer from the channel $(n_a^{(0)i}, n_b^{(0)i})$ belonging to ring i to the channels $(n_a^{(m)j}, n_b^{(m)j})$ of ring j; see eq 6.

$$kr_{ij} = \sum_{m=0}^{5} kr_{ij}^{(m)} \tag{43}$$

The energy transfer rate constant $kr_{ij}^{(m)}$ from channel $(n_a^{(0)i}, n_b^{(0)i})$ to channel $(n_a^{(m)j}, n_b^{(m)j})$ is calculated as the sum of the rate constants for energy transfer starting from the site in the middle $n_c = n_c^{max}/2$ of the channel $(n_a^{(0)i}, n_b^{(0)i})$ and ending at any site in the channel $(n_a^{(m)j}, n_b^{(m)j})$.

$$kr_{ij}^{(m)} = \sum_{n_c} k(z(n_c), r_{ij}^{(m)})$$

$$z(n_c) = uc[n_c - n_c^{max}/2] \tag{44}$$

$r_{ij}^{(m)}$ is the distance between these two channels:

$$r_{ij}^{(m)} = \sqrt{(n_a^{(0)i} - n_a^{(m)j})^2 + (n_a^{(0)i} - n_a^{(m)j})(n_b^{(0)i} - n_b^{(m)j}) + (n_b^{(0)i} - n_b^{(m)j})^2} \tag{45}$$

The distances $r_{ij}^{(m)}$ are the same when i and j are exchanged with each other. This means that kr_{ij} is equal to kr_{ji}. The energy transfer rate constant kr_{iI} from ring i to ring I is calculated analogously. The time evolution of $Pr_i(t)$ can be expressed in the same way as $Pz_i(t)$, according to eq 25.

$$Pr_i(t + \Delta t) = Pr_i(t)\Big(1 - \sum_j kr_{ij}\Delta t\Big) + \sum_j Pr_i(t)kr_{ji}\Delta t \tag{46}$$

$$Pr_I(t + \Delta t) = Pr_I(t) + \sum_i Pr_i(t)kr_{iI}\Delta t \tag{47}$$

The radial excitation distribution $\mathbf{Pr}_t$ is calculated like $\mathbf{Pz}_t$, see eqs 39, 40, and 41, by using the matrix $\mathbf{Mr}$. The elements of $\mathbf{Mr}$ correspond to those of eq 28, but the rate constants k_{ij} and k_{iI} are exchanged by kr_{ij} and kr_{iI}, respectively.

$$\mathbf{Pr}_t = \mathbf{Pr}_0 \cdot (\mathbf{Mr})^n \quad \text{with} \quad t = n\Delta t \tag{48}$$

The dimension of $\mathbf{Mr}$ is equal to the number of rings in the cylinder. The coat trapping function $T^S_C(t)$ is equal to the sum of the occupation probabilities $Pr_I(t)$ of all rings having a radius r between $(r_{max} - |\mathbf{a}|)$ and r_{max}.

$$T^S_C(t) = \sum_{r_i = r^{max} - |a|}^{r^{max}} Pr_i(t) \tag{49}$$

The axial trapping function $T^S_A(t)$ is equal to the occupation probability $Pr_0(t)$ of the central channel:

$$T^S_A(t) = Pr_0(t) \tag{50}$$

Point Trapping. To reach the trap at the center of the front of the microcrystal, the electronic excitation has to reach both the axis and the front of the cylinder. Thus, point trapping $T^S_P(t)$ is the product of axial trapping $T^S_A(t)$ and front trapping $T^S_F(t)$.

$$T^S_P(t) = T^S_A(t)\, T^S_F(t) \tag{51}$$

This concludes the calculation of the independent trapping functions, and we now consider the competition between the different trapping types and fluorescence. Supposing that in a system the whole outer surface of the cylinders is covered by traps. The electronic excitation has three different pathways to leave the system, namely, front−back trapping, coat trapping, and fluorescence. These decay pathways are governed by different properties of the system. Front−back trapping is connected with $\mathbf{Pz}$ and coat trapping is connected with $\mathbf{Pr}$, while fluorescence is independent of the excitation distribution $\mathbf{P}$.

Dye-Loaded Hexagonal Microporous Crystals

J. Phys. Chem. B, Vol. 101, No. 8, 1997 **1403**

However, the rates of all decays are proportional to the remaining excitation $P^{tot}(t)$; see eqs 31 and 34. For the independent processes, the remaining excitation $P^{tot}(t)$ is only determined by them. For front−back trapping, $T^S_{FC}(t)$, this is written as an example:

$$P^{tot}(t) = 1 - T^S_{FB}(t) \tag{52}$$

When the decays are in competition with each other, the remaining excitation, $P^{tot}(t)$, is determined by the sum of them:

$$P^{tot}(t) = 1 - T_{FB}(t) - T_C(t) - F(t) \tag{53}$$

This is included in the following equations to calculate the different trapping and fluorescence rates.

$$\frac{dT_{FB}(t)}{dt} = \frac{1 - T_{FB}(t) - T_C(t) - F(t)}{1 - T^S_{FB}(t)} \frac{dT^S_{FB}(t)}{dt}$$

$$\frac{dT_C(t)}{dt} = \frac{1 - T_{FB}(t) - T_C(t) - F(t)}{1 - T^S_C(t)} \frac{dT^S_C(t)}{dt}$$

$$\frac{dF(t)}{dt} = \frac{1 - T_{FB}(t) - T_C(t) - F(t)}{1 - F^S(t)} \frac{dF^S(t)}{dt} \tag{54}$$

The trapping functions $T_{FB}(t)$, $T_C(t)$, and $F(t)$ are determined numerically as follows:

$$F(t + \Delta t) = F(t) + \frac{dF(t)}{dt}\Delta t$$

$$T_C(t + \Delta t) = T_C(t) + \frac{dT_C(t)}{dt}\Delta t$$

$$T_{FB}(t + \Delta t) = T_{FB}(t) + \frac{dT_{FB}(t)}{dt}\Delta t \tag{55}$$

The starting point is at time $t = 0$, where electronic excitation is homogenously distributed on sites i and all the functions $T_{FB}(0)$, $T_C(0)$, and $F(0)$ are zero. In the same way, other systems are calculated where other types of trapping are in competition with fluorescence. Competition between two different types of trapping can be treated with this method if the trapping rates are based on excitation distributions along different directions. The independent trapping functions cannot be used to investigate competition between axial trapping and coat trapping, as an example because both rates are based on the radial excitation distribution **Pr**.

In the next section we evaluate numerically energy transfer rate constants, energy migration, and the trapping behavior for different situations.

3. Results and Discussion

We now apply the theory developed in the previous section to specific problems that have been found to be relevant in experimental studies of dye molecules in zeolite L. It therefore makes sense to refer to the geometrical constraints imposed by the structure of this zeolite. If not otherwise stated, the calculations are based on the following conditions: the microcrystals have equal length and diameter ($l_{cyl} = 2r_{cyl}$). The spectral overlap J_{ij} is 1.05×10^{-13} cm^3 M^{-1}, which corresponds to pyronine in zeolite L. The occupation probability p_i (see eq 1) is set equal to 0.25. Using eq 14, it is possible to convert the so obtained rate constants to any other set of J_{ij} or p_i, for

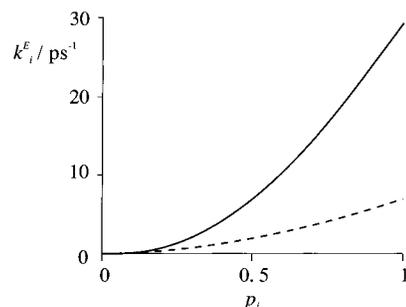| Δn_c	0 $\rightarrow$ 1	2	3
0	156	2.44	0.214
1	11.5	0.097	0.326	0.083
$\sqrt{3}$	0.425	0.048	0.011	0.016
2	0.018	0.037	0.002	0.007

Figure 4. Calculated rate constants for different situations. (Top) Energy transfer rate constants k_{ij}, in units of 10^9 s^{-1}, for jumps from the shaded site i to neighbor sites j for $p_i = 0.25$ and $J_{ij} = 1.05 \times 10^{-13}$ cm^3 M^{-1}. (Bottom) Depopulation rate constant k_i^E/ps of a site i as a function of the occupation probability p_i for $J_{ij} = 4.4 \times 10^{-13}$ cm^3 M^{-1} (solid) and for $J_{ij} = 1.05 \times 10^{-13}$ cm^3 M^{-1} (dashed).

example to $J_{ij} = 4.4 \times 10^{-13}$ cm^3 M^{-1}, which is valid for oxonine in zeolite L, or to $p_i = 1$, valid for zeolites completely filled by dye molecules. The spectral overlap J_{il} and the occupation probability p_I are set equal to J_{ij} and p_i. The luminescence lifetime τ_i is chosen to be 3.2 ns, which corresponds to pyronine in zeolite L.[31]

A 0.1 μm large microcrystal contains about 750 parallel channels. Since one ring contains six channels, their number is about 125. Each channel consists of 134 unit cells. Dye molecules with a size similar to pyronine and oxonine occupy two unit cells ($u = 2$). This means that up to 67 dye molecules find space in one channel. The number of slabs is also given by this number. The total number of dye molecules can be about 50 000 for a microcrystal of this size.

It is important to first get an impression of the rate of energy migration in such a system. We report in Figure 4 two kinds of information, namely, in the upper part individual rate constants k_{ij} from the starting site, which is shaded, to a representative selection of neighbor sites and in the lower part the energy migration rate constant k_i^E as a function of the occupation probability p_i. Energy transfer to the neighbor along the channel axes is by far the most probable event. With increasing distance z_{ij} the individual rate constants k_{ij} for energy transfer decrease strongly. The reason for this is the pronounced distance dependence of dipole−dipole interactions; see eqs 11 and 15. Energy transfer to the nearest-neighbor sites perpendicular to the channel axes is much less probable than along the channel axes. This difference is due to the orientation factor κ^2, which is very different for these two transitions, as shown in Scheme 4, and to the slightly larger distance. Due to the angular dependence of κ^2, the rate constant for the transition along the vector $(\Delta n_a, \Delta n_c) = (1,1)$ is much smaller than that along the vector $(\Delta n_a, \Delta n_c) = (1,2)$, although the former vector is shorter than the latter. All rate constants k_{ij} are proportional to the square of the occupation probability p_i^2 and to the spectral overlap J_{ij}, as stated above. The ratio between the different rate constants is therefore not affected by these parameters, and
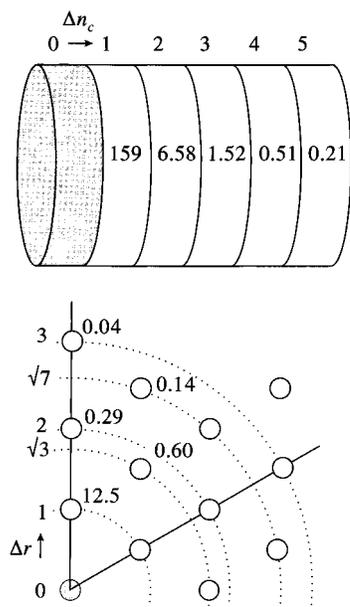
Figure 5. Calculated rate constants for $J_{ij} = 1.05 \times 10^{-13}$ cm^3 M^{-1} and $p_i = 0.25$. Δr is the distance between the channels in units of the shortest distance and Δn_C numbers the slabs with respect to the initial one. (Top) Rate constants kz_{ij} for energy transfer from the shaded slab to the neighbor slabs j. (Bottom) Rate constants kr_{ij} for energy transfer from the shaded channel to the neighbor channels j.

any sum of rate constants k_{ij} shows the same proportionalities. The energy migration rate constant k_i^E is given by a sum of rate constants k_{ij}; see eq 22. Its proportionality to p_i^2 and to J_{ij} is documented in the lower part of Figure 4. It is remarkable that the calculated energy migration rate constants reach values of up to 30 ps^{-1}. For comparison, in the antenna system of the green photosynthetic bacterium *Chloroflexus aurantiacus* energy migration constants of about 0.2 ps^{-1} have been reported.[45] In our system values of this order are possible already for relatively low occupation probabilities.

Energy migration along the channel axes is based on energy transfer between slabs, and analogously, energy migration perpendicular to it is based on energy transfer from one channel to another. The rate constants for transitions between slabs and channels, kz_{ij} and $kr_{ij}^{(0)}$, have been calculated using eqs 38 and 44 and are reported in Figure 5. These rate constants are determined by the distance between the slabs and the channels, respectively. Hence, kz_{ij} is equal to kz_{ji}, and rate constants from the shaded channel to all channels sitting on a circle around it are equal. Energy transfer to the neighbor slab is about 18 times more probable than to any other slabs. Moreover, the rate constant for transitions between neighbor slabs is close to that for transitions between neighbor sites inside one channel. This means that energy migration along the channel axes runs predominantly inside the same channel simply from one site to its neighbor. We observe a similar behavior for energy migration perpendicular to the channel axes, where energy migration runs predominantly between nearest-neighbor sites of the same slab. Comparison of the rate constants for the transition between neighbor slabs and nearest-neighbor channels shows that energy migration along the channel axes is much faster than perpendicular to it.

Energy migration causes a displacement of an electronic excitation inside a microcrystal. In Figure 6 we show the time evolution of the excitation distribution **Pz** in a row of 71 slabs when at time $t = 0$ only the slab ($n_c = 35$) in the center of this row carries an electronically excited dye molecule. Fluorescence and trapping have been excluded to simplify the descrip-
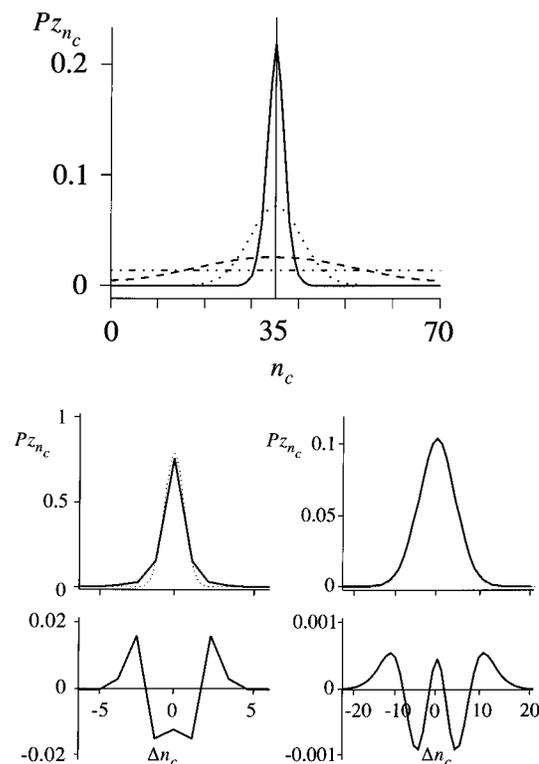

Figure 6. Transport of the electronic excitation along the channel axis of a microcrystal consisting of 71 slabs in the absence of fluorescence and traps. (Top) Excitation distribution **Pz** at 0 (line), 10 (solid), 80 (dotted), 650 (dashed), and 5200 ps (dash−dot) after irradiation in the absence of any traps and fluorescence. The electronic excitation is initially located in slab 35. (Bottom) Comparison between the calculated excitation distribution **Pz** (solid) with a Gaussian distribution (dotted) 1 ps (left) and 40 ps (right) after irradiation of site i, which is located in slab $\Delta n_C = 0$. The differences between the **Pz** and the Gaussian are plotted below the corresponding distributions.

tion of this process. The excitation distribution after 10, 80, 650, and 5200 ps is illustrated in Figure 6 (top). At time 0, immediately after irradiation, the excitation distribution **Pz**$_0$ is given by $Pz_{(n_c=35)}(0) = 1$ and $Pz_{(n_c \neq 35)}(0) = 0$. Due to energy migration the excitation distribution **Pz** becomes broader with time. In Figure 6 (bottom) the excitation distributions **Pz** calculated for 1 and 40 ps after irradiation are compared with a Gaussian $G(j,t)$. This function would correspond to the time evolution of **Pz**$_0$ if the displacement of the electronic excitation could be described by diffusion with a diffusion coefficient D.[46]

$$G(z_{ij},t) = \frac{1}{\sqrt{4\pi Dt}} e^{-z_{ij}^2/4Dt} \qquad (56)$$

It is not possible to describe **Pz**, for example, 1 ps after irradiation by a Gaussian. We have to wait at least 40 ps before such a description becomes sufficiently precise. The reason for this is the following: In a diffusion process only a movement over an infinitesimally short distance is possible during an infinitesimally short time interval. In energy migration, however, the electronic excitation is allowed to jump over a relatively long distance during an infinitesimally short time interval. After enough time has elapsed this averages out so that the excitation distribution **Pz** can be represented by a Gaussian $G(j,t)$ so that a constant diffusion coefficient D can be defined. Diffusion coefficients of up to about 0.3 cm^2 s^{-1} have been calculated at maximum loading with, for example, oxonine. This is 100 times more than in photosynthetic antenna systems, where diffusion coefficients on the order of 2×10^{-3} to 4×10^{-3} cm^2 s^{-1} have been reported.[47] The diffusion

Dye-Loaded Hexagonal Microporous Crystals

J. Phys. Chem. B, Vol. 101, No. 8, 1997 **1405**

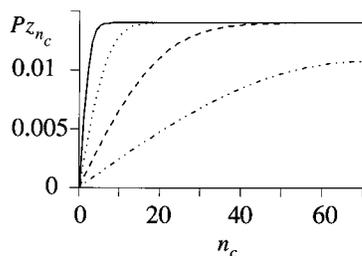**Figure 7.** Excitation distribution **Pz** along the channel axis of a microcrystal consisting of 71 slabs under the condition of equal excitation probability at $t = 0$ for all slabs in the absence of fluorescence. Traps are positioned on the front of the cylinder, that means in slab 0. Calculations have been carried out at 10 (solid), 80 (dotted), 650 (dashed), and 5200 ps (dash−dot) after irradiation.

TABLE 2: Diffusion Coefficients

J_{ij}/cm^3 M^{-1}	p_i	D/cm^2 s^{-1}
1.05×10^{-13}	0.25	4.357×10^{-3}
	1.00	6.971×10^{-2}
4.4×10^{-13}	0.25	1.826×10^{-2}
	1.00	2.921×10^{-1}

coefficient corresponds to a mean energy transfer rate constant along the cylinder axes and is thus an average of the rate constants k_{ij}. Hence, it is proportional to J_{ij} and p_i^2. The migration length l_{mig} corresponds to the mean distance that an electronic excitation can travel during the natural lifetime τ_i; see eq 56.

$$l_{mig} = \sqrt{2D\tau_i} \qquad (57)$$

l_{mig} is related to the square root of the diffusion coefficient D. This means that it is proportional to p_i and to the square root of J_{ij}:

$$l_{mig} \propto p_i$$

$$l_{mig} \propto \sqrt{J_{ij}} \qquad (58)$$

D is proportional to τ_i^{-1}, like the rate constant k_{ij} (see eq 11); hence l_{mig} is independent of τ_i. Diffusion coefficients and corresponding migration lengths l_{mig} for different values p_i of J_{ij} are given in Table 2.

The influence of trapping on the excitation distribution in the absence of fluorescence is illustrated in Figure 7 for a row of 71 slabs, where the first one, slab 0, is occupied by traps. Immediately after irradiation all slabs have the same excitation probability Pz_{n_c}. The excitation distribution **Pz** is depicted in Figure 7 at 10, 80, 650, and 5200 ps after irradiation. The slabs i near the trapping slab 0 very quickly lose electronic excitation, because only one or only a few energy transfer steps are required to reach the traps. The trapping rate dT/dt is proportional to the gradient of **Pz** at the position of the traps. Hence, dT/dt depends not only on the remaining excitation $P^{tot}(t)$ but also on the excitation distribution **P**. This is in contrast to the fluorescence rate dF/dt, which depends only on $P^{tot}(t)$.

The independent front trapping function $T^S_F(t)$ has been calculated for similar systems as above and also the other independent trapping functions, e.g. $T^S_{FB}(t)$ and $T^S_C(t)$, have been evaluated. More interesting are the results for systems in which different types of trapping and fluorescence are in competition with each other. The systems under investigation differ by the position of the traps on the outer surface. In the first one the whole surface of a cylinder is covered by traps; hence front−back trapping, coat trapping, and fluorescence are in competition with each other. The second one consists of microcrystals, in
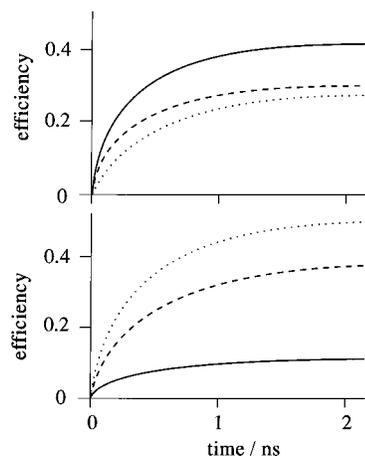

Figure 8. Competition between front trapping $T_F(t)$ (solid), coat trapping $T_C(t)$ (dashed), and fluorescence $F(t)$ (dotted) in a cylinder of 100 nm length and diameter with $p_i = 0.25$ and $J_{ij} = 1.05 \times 10^{-13}$ cm^3 M^{-1}, for parallel and for isotropic orientation of the chromophores. (Top) Parallel orientation of transition dipole moments. (Bottom) Random (isotropic) orientation of the transition dipole moments.

which only the front is covered by traps. Here, the competing reactions are front trapping and fluorescence. In the third one, the efficiency of one single trap positioned in the center of the front is investigated, which is competing with fluorescence. This efficiency is compared with efficiencies of single traps positioned at an arbitrary position either on the front or on the coat of the cylinder.

The trapping functions $T_{FB}(t)$, $T_C(t)$, and $F(t)$ of the first system have been calculated for the usual conditions and are plotted in Figure 8. In the upper part, the transition dipoles of all dye molecules have been assumed to be parallel, while in the lower part isotropic orientation has been applied. Under the anisotropic conditions, traps on the front or the back gain electronic excitation faster than traps on the coat. Front−back trapping is therefore more efficient than coat trapping, while fluorescence is the least efficient process. Under isotropic conditions, however, fluorescence is the most efficient process, coat trapping is only slightly affected by this change of conditions, and front−back trapping is the least efficient process. To explain these results qualitatively, let us consider the mean distance that excitation has to pass to reach its nearest trap. We call it the trapping distance. As for front−back trapping, the distances between slabs i and their nearest trapping slab I range from 0 to $l_{cyl}/2$. All these distances have the same weight. From this, the trapping distance for front−back trapping is $l_{cyl}/4$. For coat trapping, distances range from 0 to r_{cyl}. Since there are much more channels close to the periphery, the small distances have a larger weight. We get a trapping distance of $r_{cyl}/3$, which corresponds to $l_{cyl}/6$, if $l_{cyl} = 2r_{cyl}$. Hence, the trapping distance for front−back trapping is 1.5 times larger than for coat trapping. Front−back trapping, however, is more efficient than coat trapping under anisotropic conditions, because energy migration along the channel axes is much faster than perpendicular to it; see Figure 5. Energy migration is so fast that the electronic excitation reaches a trap in a time shorter than τ_i. Hence, the losses by fluorescence are low. Under isotropic conditions the angular dependence supporting energy migration along the channel axes is no longer valid and the influence of the different trapping distances increases. This means that in this case coat trapping is much more efficient than front trapping. The larger losses by fluorescence indicate that energy migration is slower than under anisotropic conditions. Coat and front−back trapping efficiencies and the fluorescence quantum yield for

TABLE 3: Coat and Front−Back Trapping Efficiencies and Fluorescence Quantum Yield for Different Spectral Overlaps, Occupation Probability, and Length of the Cylinder[a]

l_{cyl}/nm	$J_{ij} = 1 \times 10^{-13}$/cm³ M⁻¹, $p_i = 0.25$			$J_{ij} = 4.4 \times 10^{-13}$/cm³ M⁻¹, $p_i = 1$		
	$T_{FB,\infty}$	$T_{C,\infty}$	Φ_F	$T_{FB,\infty}$	$T_{C,\infty}$	Φ_F
			$r_{cyl} = 53$ nm			
50	0.677	0.188	0.134	0.757	0.204	0.038
100	0.43	0.302	0.268	0.544	0.367	0.089
150	0.297	0.359	0.344	0.398	0.475	0.127
200	0.218	0.393	0.389	0.3	0.547	0.153
250	0.174	0.412	0.414	0.242	0.59	0.138
			$l_{cyl} = 2r_{cyl}$			
37	0.566	0.37	0.064	0.606	0.393	0.001
51	0.539	0.357	0.105	0.604	0.394	0.002
74	0.495	0.338	0.168	0.6	0.397	0.003
106	0.403	0.313	0.283	0.571	0.422	0.007
			Isotropic Arrangement of the Dye Molecules			
106	0.115	0.383	0.502			

[a] For comparison, the trapping efficiencies and the fluorescence quantum yield are given for isotropic arrangement of the dye molecules.
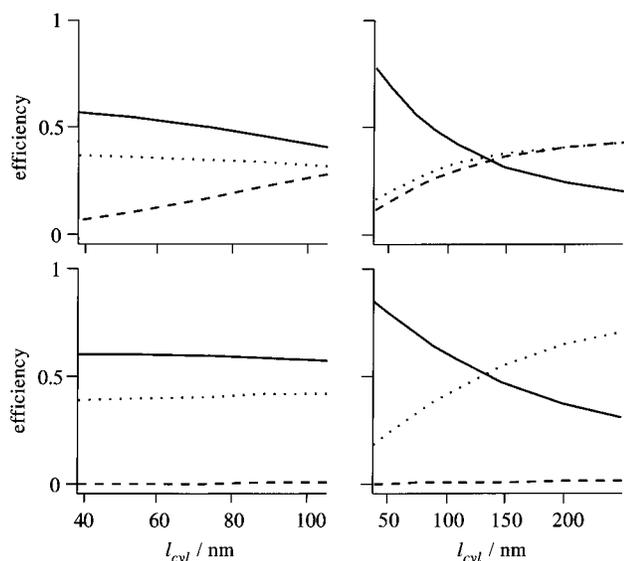

Figure 9. Efficiencies of front−back trapping $T_{FB,\infty}$ (solid), coat trapping $T_{C,\infty}$ (dotted), and fluorescence (dashed) as a function of the length of the cylinder for two different geometries. (Left) $r_{cyl} = 0.5l_{cyl}$. (Right) ($r_{cyl} = 100$ nm). The results shown in the upper cases have been calculated for $J_{ij} = 1.05 \times 10^{-13}$ cm³ M⁻¹, $p_i = 0.25$ and those at the bottom with $J_{ij} = 4.4 \times 10^{-13}$ cm³ M⁻¹, $p_i = 1$.

anisotropic and isotropic arrangement of the dye molecules are given in Table 3.

The efficiencies of front−back and coat trapping and the fluorescence quantum yield have been studied as a function of the microcrystals' size and shape for two different sets of p_i and J_{ij}. The results are documented in Figure 9 and Table 3. In the upper part of Figure 9, the calculations have been performed under the usual conditions, and in the lower part for $p_i = 1$ and $J_{ij} = 4.4 \times 10^{-13}$cm³ M⁻¹. On the left side of Figure 9, the size of the microcrystals has been varied ($l_{cyl} = 2r_{cyl}$), and on the right side only l_{cyl} has been varied, while r_{cyl} was kept constant ($r_{cyl} = 53$ nm). The fluorescence quantum yield increases with increasing size of the cylinders due to the increasing trapping distance. This effect is less pronounced under the faster conditions, where the fluorescence quantum yield remains close to zero, even in microcrystals with l_{cyl} of up to 250 nm and r_{cyl} of up to 100 nm. Increasing l_{cyl} provides larger differences between the trapping distances for front−back trapping than for coat trapping, for $l_{cyl} = 2r_{cyl}$ as well as for constant r_{cyl}. This means that the front trapping efficiency decreases and the coat trapping efficiency increases with

TABLE 4: Front Trapping Efficiency for Different Cylinder Length

	$T_{F,\infty}$			
	$J_{ij} = 1 \times 10^{-13}$ cm³ M⁻¹		$J_{ij} = 4.4 \times 10^{-13}$ cm³ M⁻¹	
l_{cyl}/nm	$p_i = 0.25$	$p_i = 1$	$p_i = 0.25$	$p_i = 1$
50	0.622	0.961	0.861	0.99
100	0.348	0.872	0.641	0.964
150	0.227	0.769	0.475	0.929
200	0.171	0.687	0.377	0.896
250	0.137	0.619	0.311	0.863

increasing l_{cyl}. The ratio between the efficiencies of coat and front−back trapping depends only on geometrical constraints and is independent of p_i or J_{ij}.

Trapping efficiencies close to 1 are possible in our system. The size of the microcrystals allowing so high efficiencies depends on p_i or J_{ij}, of course. Under usual conditions, the microcrystals should not be longer than 50 nm. Under the faster conditions, however, microcrystals with a length of up to 250 nm and a diameter of up to 100 nm still provide very high trapping efficiencies. Disklike structures are more favorable than cigar-like structures. High trapping efficiencies have been observed experimentally.[31]

In the second system, only the front of a cylindrical microcrystal is covered with traps. To obtain such a system, microcrystals have to be arranged on a plain substrate surface, all standing with the front side on it. Front trapping efficiency $T_{F,\infty}$ corresponds to the probability that the energy of a photon absorbed in the microcrystal reaches the substrate surface to cause a designed reaction there. The influences of J_{ij}, p_i, and the length l_{cyl} of the microcrystals on this efficiency have been calculated and are given in Figure 10 and Table 4. Energy migration perpendicular to the channel axes is not relevant because no traps are positioned on the coat. Thus, the diameter of the microcrystal plays no role.

This study enables us to find systems with front trapping efficiencies above a certain limit. Let us give two examples: Front trapping efficiencies close to 1 are possible in microcrystals with $l_{cyl} = 50$ nm, completely filled with dye molecules ($p_i = 1$) having a spectral overlap of more than 1×10^{-13} cm³ M⁻¹. Efficiencies of more than 0.85 are supported in cylinders of up to 250 nm length, completely filled with dye molecules having a spectral overlap of 4×10^{-13} cm³ M⁻¹. Other conditions are easily deduced using Figure 10. We distinguish between systems where the migration length l_{mig} of electronic excitation is longer and systems where it is shorter than l_{cyl} to explain qualitatively the dependences of $T_{F,\infty}$. Migration lengths

Dye-Loaded Hexagonal Microporous Crystals

J. Phys. Chem. B, Vol. 101, No. 8, 1997 **1407**

TABLE 5: Point Trapping Efficiency for Different Cylinder Lengths and Comparison between the Efficiencies of a Single Trap in the Center of the Front, at an Arbitrary Position on the Front and the Back, and at an Arbitrary Position on the Coat

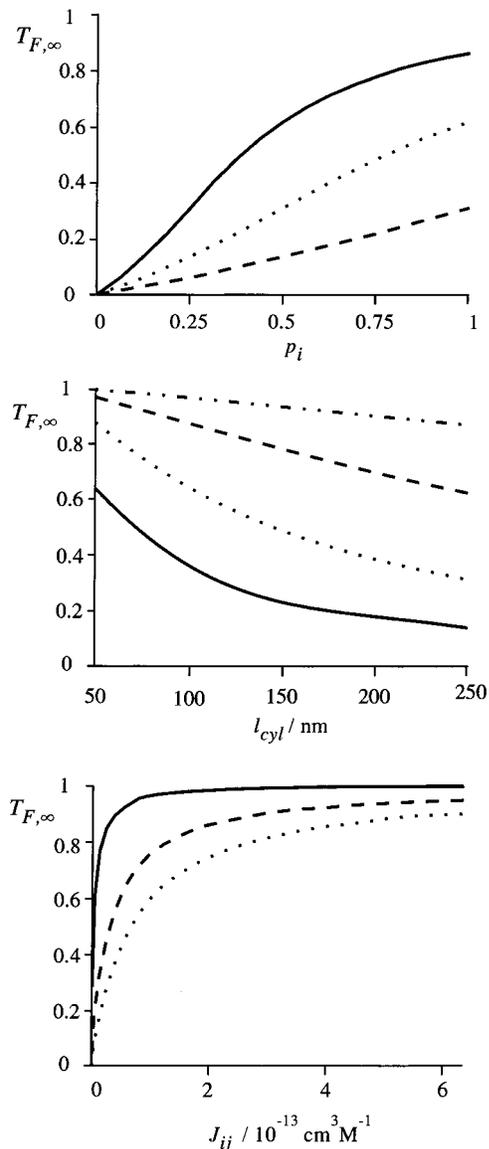| l_{cyl}/nm $l_{cyl} = 2r_{cyl}$	$J_{ij} = 1 \times 10^{-13}$ cm^3 M^{-1}		$J_{ij} = 4.4 \times 10^{-13}$ cm^3 M^{-1}		$J_{ij} = 1 \times 10^{-13}$ cm^3 M^{-1}, $p_i = 0.25$	
	$p_i = 0.25$ $T_{P,\infty}$	$p_i = 1$ $T_{P,\infty}$	$p_i = 0.25$ $T_{P,\infty}$	$p_i = 1$ $T_{P,\infty}$	$T_{FB,\infty}$	$T_{C,\infty}$
37	0.282	0.87	0.63	0.965	0.048	0.022
51	0.148	0.77	0.44	0.93	0.021	0.009
74	0.062	0.58	0.25	0.85	0.006	0.003
106	0.019	0.28	0.085	0.61	0.002	0.001

Figure 10. Influence of the length of the microcrystals, the occupation probability, and the spectral overlap on the front trapping efficiency. (Top) $T_{F,\infty}$ as a function of p_i for different spectral overlaps. The length of the cylinder was 250 nm. $J_{ij} = 4.4 \times 10^{-13}$ cm^3 M^{-1} (solid), $J_{ij} = 1 \times 10^{-13}$ cm^3 M^{-1} (dotted), $J_{ij} = 2.5 \times 10^{-14}$ cm^3 M^{-1} (dashed). (Middle) $T_{F,\infty}$ as a function of the length of the cylinder for two different occupation probabilities and two spectral overlaps. $p_i = 0.25$: $J_{ij} = 1 \times 10^{-13}$ cm^3 M^{-1} (solid) and $J_{ij} = 4.4 \times 10^{-13}$ cm^3 M^{-1} (dashed). $p_i = 1$: $J_{ij} = 1 \times 10^{-13}$ cm^3 M^{-1} (dotted) and $J_{ij} = 4.4 \times 10^{-13}$ cm^3 M^{-1} (dash−dot). (Bottom) $T_{F,\infty}$ as a function of the spectral overlap J_{ij} for $p_i = 1$ and three different lengths of the cylinder: $l_{cyl} = 50$ nm (solid), $l_{cyl} = 150$ nm (dotted), $l_{cyl} = 250$ nm (dashed).

l_{mig} are given in Table 2. In the first group of systems, increasing l_{cyl} causes a decrease of $T_{F,\infty}$ due to larger trapping distances. Decreasing p_i and J_{ij} both reduces the energy migration rate constant so that electronic excitation needs more time to reach the traps. This causes a decrease of $T_{F,\infty}$. In the
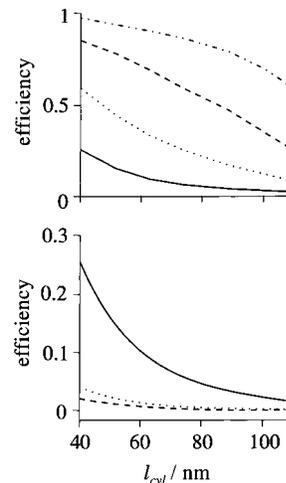

Figure 11. Influence of the length of the microcrystals, of the occupation probability, and of the spectral overlap on the point trapping efficiency, and comparison of the point trapping, the front trapping, and the coat trapping efficiencies. (Top) $T_{P,\infty}$ as a function of l_{cyl} for two different occupation probabilities and two spectral overlaps. $p_i = 0.25$: $J_{ij} = 1 \times 10^{-13}$ cm^3 M^{-1} (solid) and $J_{ij} = 4.4 \times 10^{-13}$ cm^3 M^{-1} (dashed). $p_i = 1$: $J_{ij} = 1.05 \times 10^{-13}$ cm^3 M^{-1} (dotted) and $J_{ij} = 4.4 \times 10^{-13}$ cm^3 M^{-1} (dash−dot). (Bottom) $T_{P,\infty}$ (solid), $T_{F,\infty}$ (dotted), and $T_{C,\infty}$ (dashed) as a function of l_{cyl}. $T_{FB,\infty}$ and $T_{C,\infty}$ have been calculated by placing one trap at an arbitrary position on the front and the back and at an arbitrary position on the coat, respectively.

other group of systems, the only electronic excitations that are able to reach traps immediately after irradiation are those for which the distance to the front is smaller than l_{mig}. The number of slabs within this distance from the trapping slab remains unaffected by a further increase of l_{cyl}. The probability that electronic excitation is initially positioned on these slabs, however, decreases with increasing l_{cyl}. Hence, the front trapping efficiency is inversely proportional to l_{cyl}. This can be seen in Figure 10 (middle) for the systems with $p_i = 0.25$. The number of such slabs, however, is determined by l_{mig}. Front trapping efficiency is therefore proportional to p_i and to the square root of J_{ij}; see eq 58. This can be seen in Figure 10 (top) for $J_{ij} < 4 \times 10^{-13}$ cm^3 M^{-1} or for $p_i < 0.25$. The shape of the cylindrical microcrystals has no influence on the front trapping efficiency. It is, however, easier to arrange disklike microcrystals with the front on a surface than cigar-like ones.

The efficiency of a single trap on the surface of the microcrystals is illustrated in Table 5 and Figure 11. In the upper part of this figure, the trap is positioned at the center of the front of the cylindrical microcrystals. This trapping type is called point trapping. The dependence of point trapping efficiency on the microcrystals' size is calculated for different sets of J_{ij} and p_i. In the lower part of Figure 11 (bottom) point trapping efficiency is compared with the efficiency of a single trap at an arbitrary position either on the front or on the coat of the cylinder. These efficiencies have been obtained by calculating front and coat trapping in competition with fluorescence, respectively. Appropriate occupation probabilities p_I of sites I have been used to allow only one trap per microcrystal. Hence,

in contrast to the default conditions, here the occupation probabilities p_l and p_i differ from each other. In microcrystals with a length and a diameter of 37 nm the point trapping efficiency is 0.28 under default conditions. Point trapping efficiencies of up to 0.965, however, are possible in microcrystals of the same size at maximum loading with, for example, oxonine. Although there exist about 12 600 chromophores in such a microcrystal, electronic excitation is transferred with a probability of nearly 1 to the single trap at the center of the front. This result, however, points to the fact that even a small amount of impurities acting as traps inside the microcrystal could quench electronic excitation very efficiently. The mean efficiencies of single traps at arbitrary positions on either the front or the coat are 0.048 and 0.022, respectively, under default conditions in microcrystals of the same size. This is much less than the corresponding point trapping efficiency.

We conclude that energy migration in optimized dye-loaded hexagonal microporous crystals can be extremely fast. Energy migration rate constants of up to 30 ps^{-1} have been calculated. They are much larger than the measured rate constants of 0.2 ps^{-1} reported in the literature for natural antenna systems. The large rate constants are encouraging for designing systems with one or several traps at the outer surface of appropriate dye-loaded zeolite microcrystals with trapping efficiencies close to 1. In zeolite L microcrystals with a length and a diameter of 50 nm, completely filled with well chosen dye molecules and the whole surface covered by traps, as an example, an electronic excitation reaches a trap with a probability of more than 99.8%. A simplifying assumption made in this study is that the individual energy transfer steps occur from thermalized states. Deviations from this are expected to play a role for rate constants above a certain limit. Furthermore the distances between the molecules become very short as we approach an occupation probability of 1. It is therefore important to design the system in a way that orbital overlaps remain negligible even at $p = 1$, which seems to be possible. Experimental studies on energy migrations in dye-loaded microcrystals as a function of the temperature, the loading, and the spectral overlap, which are in progress in our laboratory, will provide further information on this exciting system.

References and Notes

(1) Cracknell, R. F.; Gubbins, K. E.; Maddox, M.; Nicholson, D. *Acc. Chem. Res.* **1995**, *28*, 281.

(2) Suib, S. L. *Chem. Rev.* **1993**, *93*, 803.

(3) Meier, W. M.; Olson, D. H.; Baerlocher, Ch. *Atlas of Zeolite Structure Types*; Elsevier: London, 1996.

(4) Cox, S. D.; Gier, T. E.; Stucky, G. D.; Bierlein, J. *J. Am. Chem. Soc.* **1988**, *110*, 2986.

(5) Werner, L.; Caro, J.; Finger, G.; Kornatowski, J. *Zeolites* **1992**, *12*, 658.

(6) Schulz-Ekloff, G. In *Advanced Zeolite Science and Applications, Studies in Surface Science and Catalysis, Vol. 85*; Jansen, J. C., Stöcker, M., Karge, H. G., Weitkamp J., Eds.; Elsevier: Amsterdam, 1994; p 145.

(7) Ehrl, M.; Deeg, F. W.; Bräuchle, C.; Franke, O.; Sobbi, A.; Schulz-Ekloff, G.; Wöhrle, D. *J. Phys. Chem.* **1994**, *98*, 47.

(8) Schüth, F. *Chemie Z.* **1995**, *29*, 42.

(9) Hoppe, R.; Schulz-Ekloff, G.; Wöhrle, D.; Kirschhock, Ch.; Fuess, H. In *Zeolites and Related Microporous Materials: State of the Art 1994. Studies in Surface Science and Catalysis, Vol. 84*; Weitkamp, J., Karge, H. G., Pfeifer, H., Hölderich, W., Eds.; Elsevier: Amsterdam, 1994; p 821.

(10) Caro, J.; Marlow, F.; Wübbenhorst, M. *Adv. Mater.* **1994**, *6*, 413.

(11) Wöhrle, D.; Schulz-Ekloff, G. *Adv. Mater.* **1994**, *6*, 875.

(12) Müller, B.; Calzaferri, G. *J. Chem. Soc., Faraday Trans.* **1996**, *92*, 1633.

(13) Calzaferri, G.; Gfeller, N. *J. Phys. Chem.* **1992**, *96*, 3428.

(14) Lainé, P.; Lanz, M.; Calzaferri, G. *Inorg. Chem.* **1996**, *35*, 3514.

(15) Fetisova, Z. G.; Freiberg, A. M.; Timpmann, K. E. *Nature* **1988**, *334*, 633.

(16) Denti, G.; Campagna, S.; Sabatino, L.; Serroni, S.; Ciano, M.; Balzani V. In *Photochemical Conversion and Storage of Solar Energy*; Pelizzetti, E., Schiavello, M., Eds.; Kluwer Academic Publishers: Dordrecht, 1991; p 27.

(17) Balzani, V.; Campagna, S.; Denti, G.; Juris, A.; Serroni, S.; Venturi, M. *Sol. Energy Mater. Sol. Cells* **1995**, *38*, 159. Balzani, V.; Campagna, S.; Denti, G.; Juris, A.; Serroni, S.; Venturi, M. *Coord. Chem. Rev.* **1994**, *132*, 1.

(18) Jullien, L.; Canceill, J.; Valeur, B.; Bardez, E.; Lehn, J.-M. *Angew. Chem.* **1994**, *106*, 2582.

(19) Bücher, H.; Drexhage, K. H.; Fleck, M.; Kuhn, H.; Möbius, D.; Schäfer, F. P.; Sondermann, J.; Sperling, W.; Tillmann, P.; Wiegand, J. *Mol. Cryst.* **1967**, *2*, 199.

(20) Willig, F. In *Photochemical Conversion and Storage of Solar Energy*; Pelizzetti, E., Schiavello, M., Eds.; Kluwer Academic Publishers: Dordrecht, 1991; p 235.

(21) Tamai, N.; Yamazaki, T.; Yamazaki, I. *J. Phys. Chem.* **1987**, *91*, 841.

(22) Pescatore, J. A., Jr.; Yamazaki, I. *J. Phys. Chem.* **1996**, *100*, 13333.

(23) Gregg, B. A.; Resch, U. *J. Photochem. Photobiol, A: Chem.* **1995**, *87*, 157.

(24) Webber, S. E. *Chem. Rev.* **1990**, *90*, 1469.

(25) Watkins, D. M.; Fox, M. A. *J. Am. Chem. Soc.* **1996**, *118*, 4344.

(26) Sturmer, D. M.; Heseltine, D. W. In *The Theory of the Photographic Process*; James, T. H., Ed.; Macmillan Publishing Co.: New York, 1977; p 194.

(27) Vlachopoulos, N.; Liska, P.; Augustynski, J.; Grätzel, M. *J. Am. Chem. Soc.* **1988**, *110*, 1216.

(28) Bignozzi, C. A.; Argazzi, R.; Schoonover, J. R.; Meyer, G. J.; Scandola, F. *Sol. Energy Mater. Sol. Cells* **1995**, *38*, 187.

(29) Kasha, M.; Rawls, H. R.; Ashraf El-Bayoumi, M. *Pure Appl. Chem.* **1965**, *11*, 371.

(30) Kühlbrandt, W.; Wang, D. N. *Nature* **1991**, *350*, 130.

(31) Binder, F.; Calzaferri, G.; Gfeller, N. *Sol. Energy Mater. Sol. Cells* **1995**, *38*, 175. Binder, F.; Calzaferri, G.; Gfeller, N. *Proc. Indian Acad. Sci (Chem. Sci.)* **1995**, *107*, 753.

(32) Ernst, S.; Weitkamp, J. *Catal. Today* **1994**, *19*, 27.

(33) Tsapatsis, M.; Okubo, T.; Lovallo, M.; Davis, M. E. *Mat. Res. Soc. Symp. Proc.* **1995**, *371*, 21.

(34) Grabowska, J.; Sienicki, K. *Chem. Phys.* **1995**, *192*, 89.

(35) Anfinrud, P.; Crackel, R. L.; Struve, W. S. *J. Phys. Chem.* **1984**, *88*, 5873.

(36) Zumofen, G.; Blumen, A. *J. Chem. Phys.* **1982**, *76*, 3713.

(37) Wolber, P. K.; Hudson, B. S. *Biophys. J.* **1979**, *28*, 197.

(38) Förster, T. *Ann. Phys (Leipzig)* **1948**, *2*, 55.

(39) Haan, S. W.; Zwanzig, R. *J. Chem. Phys.* **1978**, *68*, 1879.

(40) Ediger, M. D.; Fayer, M. D. *Int. Rev. Phys. Chem.* **1985**, *4*, 207.

(41) Loring, R. F.; Andersen, H. C.; Fayer, M. D. *J. Chem. Phys.* **1984**, *80*, 5731.

(42) Keller, L.; Hussey, D. M.; Fayer, M. D. *J. Phys. Chem.* **1996**, *100*, 10257.

(43) Scholes, G. D.; Ghiggino, K. P. *J. Chem. Phys.* **1995**, *103*, 8873.

(44) Förster, Th. *Fluoreszenz Organischer Verbindungen*; Vandenhoeck & Ruprecht: Göttingen, 1951.

(45) Savikhin, S.; Zhu, Y.; Blankenship, R. E.; Struve, W. S. *J. Phys. Chem.* **1996**, *100*, 3320.

(46) Atkins, P. W. *Physical Chemistry*, 5th ed.; Oxford University Press: Oxford, 1994; p 853.

(47) Rubin, L. B.; Braginskaya, O. V.; Isakova, M. L.; Efremov, N. A. *Photochem. Photobiol.* **1985**, *42*, 77.